

# Effect of defects on phonons and the effective spin-spin interactions of an ultracold Penning-trap quantum simulator

M. McAneny, B. Yoshimura, and J. K. Freericks

*Department of Physics, Georgetown University, 37th and O Streets NW, Washington, DC 20057, USA*

(Received 6 September 2013; published 30 October 2013)

We generalize the analysis of the normal modes for a rotating ionic Coulomb crystal in a Penning trap to allow for inhomogeneities in the system. Our formal developments are completely general, but we choose to examine a crystal of  $\text{Be}^+$  ions with  $\text{BeH}^+$  defects to compare with current experimental efforts. We examine the classical phonon modes (both transverse and planar) and we determine the effective spin-spin interactions when the system is driven by an axial spin-dependent optical dipole force. We examine situations with up to approximately 15% defects. We find that most properties are not strongly influenced by the defects, indicating that the presence of a small number of defects will not significantly affect experiments.

DOI: 10.1103/PhysRevA.88.043434

PACS number(s): 37.10.Ty, 03.67.Pp, 03.67.Ac, 03.67.Lx

## I. INTRODUCTION

Current work on quantum-mechanical simulators is motivated by Feynman's 1982 proposal [1]. One of the most successful systems for engineering model spin systems (which evolve naturally and whose properties can be measured directly) is ion trap emulators [2–10]. These systems are advantageous because of their long decoherence times, precise spin-state quantum control, and high-fidelity readout. But most experiments have not yet reached system sizes where they are superior to conventional digital computer calculations (for example, linear Paul-trap experiments have worked with as many as 16 spins [10] in a one-dimensional linear crystal). However, using a Penning trap, researchers at NIST have created systems of  $\sim 300$  spins in a single-plane two-dimensional crystal and have demonstrated the use of a spin-dependent optical dipole force to realize tunable Ising-type spin-spin couplings, which is an important first step in the simulation of quantum magnetism in systems that are intractable using conventional computers [7,8].

One complication to the NIST experiment is the accumulation of impurities in the crystal during the experimental procedure. Hydrogen molecules and water molecules in the background gas collide with the beryllium ions in the crystal and form a variety of impurities [11], the most common being  $\text{BeH}^+$  ions or  $\text{BeOH}^+$  ions ( $\text{H}^+$  ions can also form as defects if the electron impact ionization electrons have too high an energy or the system is at too high a temperature; but when that happens, the crystal is usually reloaded, so we neglect them). In this article, we generalize previous work for the normal modes in a Penning trap [12] to include these types of defects. In our numerical calculations, we focus solely on the  $\text{BeH}^+$  defects (which are the most commonly seen defect), although the generalization to other defects is a straightforward and simple task. Because these defects are more massive than the  $\text{Be}^+$  ions, they are centrifugally driven to the boundary of the planar array. We determine how these defects affect the eigenfrequencies and eigenvectors of the normal modes, and investigate how these changes affect the spin-spin interactions when detuning the optical dipole force to the blue of the axial center-of-mass mode.

The organization of the paper is as follows. In Sec. II, we generalize the theory for the normal modes of cold ions in a

Penning trap to include the presence of impurities. In Sec. III, we provide representative numerical examples to illustrate how  $\text{BeH}^+$  defects modify the phonon frequencies and the spin-spin interactions. In Sec. IV, we provide our conclusions.

## II. THEORETICAL FORMULATION FOR A PENNING TRAP WITH DEFECTS

We consider a collection of ions formed as a two-dimensional crystal in a Penning trap as shown in Fig. 1. Previous work [12] considered a homogeneous crystal of  ${}^9\text{Be}^+$  ions, constructing the Lagrangian for the system and transforming to a corotating frame to remove the time dependence from the Lagrangian in order to treat the problem as a static equilibrium problem. When allowing for the possibility of defects, the only change to this formulation is to include an index for the mass degree of freedom, allowing it to change from site to site. Thus, the Lagrangian in the rotating frame for any collection of ions is (the superscript  $R$  denotes the rotating frame)

$$L^R = \sum_{j=1}^N \left[ \frac{1}{2} m_j |\dot{\mathbf{r}}_j^R|^2 - \frac{eB^{\text{eff}}[j, \omega]}{2} (\dot{x}_j^R y_j^R - \dot{y}_j^R x_j^R) - e\phi_j^R \right], \quad (1)$$

where  $N$  is the total number of ions,  $B^{\text{eff}}[j, \omega] = B_z - 2\omega m_j/e$  is the effective magnetic field in the rotating frame,  $\omega > 0$  is the angular rotation frequency of the crystal ( $\Omega = -\omega \hat{z}$ ),  $m_j$  is the mass of ion  $j$ ,  $e$  is the positive unit charge, and  $\mathbf{r}_j^R$  is the position vector from the origin of the plane to the  $j$ th ion. We use both Cartesian coordinates  $\mathbf{r}_j^R = (x_j^R, y_j^R, z_j^R)$  and cylindrical coordinates, where  $\rho_j^R = \sqrt{(x_j^R)^2 + (y_j^R)^2}$ , in our formulas. The effective potential satisfies

$$\begin{aligned} e\phi_j^R = & eV_0 z_j^{R2} + \frac{1}{2}(eB_z\omega - m_j\omega^2 - eV_0)\rho_j^{R2} \\ & + eV_W(x_j^{R2} - y_j^{R2}) + \frac{k_e e^2}{2} \sum_{k \neq j} \frac{1}{r_{jk}^R}, \end{aligned} \quad (2)$$

with  $V_0$  the amplitude of the Penning-trap electrodes,  $V_W$  the amplitude of the rotating wall potential, and  $r_{jk}^R = |\mathbf{r}_j^R - \mathbf{r}_k^R|$  the interparticle distance between ions  $j$  and  $k$ . In this frame, the centrifugal force originates from the term  $-\frac{1}{2}m\omega^2\rho_j^{R2}$  in

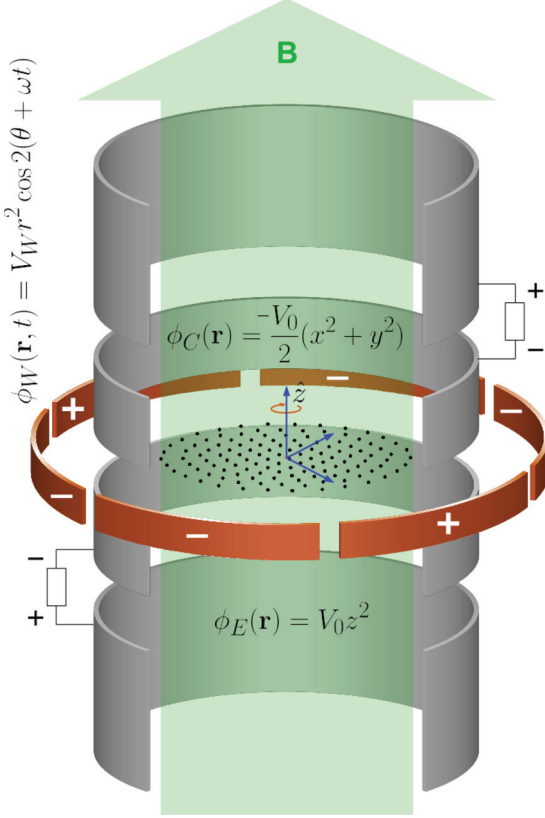


FIG. 1. (Color online) Electrostatic potentials provided by electrodes in a Penning trap have contributions from both the end-cap electrodes [with the trapping potential  $\phi_E(\mathbf{r}) = V_0 z^2$  that pushes the atoms towards  $z = 0$ ] and the cylindrical electrodes [with the radial quadratic potential  $\phi_C(\mathbf{r}) = -\frac{V_0}{2}(x^2 + y^2)$ , which tends to push the ions out radially]. In addition, the repulsive Coulomb potential between the ions tends to destabilize the system in the trap. A static magnetic field  $\mathbf{B} = B_z \hat{z}$  ( $B_z > 0$ ) is thus applied along the axial direction to provide the radial confinement of the ions. To lock the rotational angular frequency of the ions at a specific rotational speed, a time-dependent clockwise quadrupole potential  $\phi_W(t) = V_W r^2 \cos 2(\theta + \omega t)$  ( $\omega > 0$ ) is applied to the ions through ring electrodes so that the steady state of the ions (with a rigid body rotational speed  $\omega$ ) can be phase locked. Note that the rotating quadrupole potential is well implemented by ring electrodes with just six sectors (as employed in the NIST Penning traps [7,13,14]).

the effective potential energy  $e\phi_j^R$ . Details for how to derive this formula can be found from a simple generalization of the derivation in Ref. [12].

### A. Equilibrium structure and normal modes in the rotating frame

We solve for the equilibrium structure of the crystal in a standard way [12,15,16], constructing initial “shell” configu-

rations and minimizing the effective potential in the rotating frame. We express all distances in terms of a characteristic length, denoted  $\ell_0$ , which satisfies

$$\ell_0 = \sqrt[3]{\frac{2ke^2}{m_{\text{Be}^+}\omega_z^2}} = \sqrt[3]{\frac{ke^2}{eV_0}}. \quad (3)$$

However, for crystals with defects, we solve the problem in a three-step fashion: (i) First we solve the pure case, with all masses equal. (ii) Next, we replace the ion located farthest from the center with a defect and re-solve for the stable equilibrium positions starting from the current ion positions. (iii) Then we iteratively continue until the chosen number of total defects,  $N_d$ , is reached. We choose this procedure when the defect ions are heavier than the majority ions, since the centrifugal force will push the heavier ions to the periphery of the crystal. (A simple generalization, which places lighter ions in positions closest to the center of the trap, would be used for lighter defects such as  $H^+$  ions if one wanted to study such a system.)

After solving for the equilibrium structure given by the equilibrium lattice site positions  $\{\mathbf{R}_j^0, j = 1 \dots, N\}$ , we expand the Lagrangian about this configuration to quadratic order with  $\mathbf{r}_j^R = \mathbf{R}_j^0 + \delta\mathbf{R}_j(t)$  (see Ref. [12] for details). The Lagrangian governing the axial motion decouples from the Lagrangian of the planar motion, yielding

$$L_{\text{ph}}^A = \frac{1}{2} \sum_{j=1}^N m_j \delta \dot{R}_j^z \delta \dot{R}_j^z - \frac{1}{2} \sum_{j,k=1}^N K_{jk}^{zz} \delta R_j^z \delta R_k^z, \quad (4)$$

in which the symmetric stiffness matrix  $\mathbf{K}^{zz}$  is a real Hermitian matrix  $K_{jk}^{zz} = K_{kj}^{zz}$  whose matrix elements are given by

$$K_{jk}^{zz} = \begin{cases} 2eV_0 - \sum_{l=1, l \neq j}^N \frac{k_e e^2}{(R_{lj}^0)^3}, & j = k \\ \frac{k_e e^2}{(R_{jk}^0)^3}, & j \neq k, \end{cases} \quad (5)$$

where  $R_{jk}^0 = |\mathbf{R}_j^0 - \mathbf{R}_k^0|$  is the distance between two ions in equilibrium (in the rotating frame). Similarly, we derive the Lagrangian for the planar normal modes to be

$$L_{\text{ph}}^P = \frac{1}{2} \sum_{j=1}^N \sum_{\alpha} m_j (\delta \dot{R}_j^{\alpha})^2 - \frac{1}{2} \sum_{j,k=1}^N \sum_{\alpha\beta} K_{jk}^{\alpha\beta} \delta R_j^{\alpha} \delta R_k^{\beta} + \sum_j^N \frac{eB^{\text{eff}}[j, \omega]}{2} [\delta R_j^x \delta \dot{R}_j^y - \delta R_j^y \delta \dot{R}_j^x], \quad (6)$$

where  $\alpha$  and  $\beta$  run over the  $x$  and  $y$  degrees of freedom only. The real Hermitian stiffness matrix  $\mathbf{K}^{\alpha\beta}$  satisfies the relation  $K_{jk}^{\alpha\beta} = K_{kj}^{\alpha\beta} = K_{jk}^{\beta\alpha} = K_{kj}^{\beta\alpha}$  (note that the Roman indices denote lattice sites, while the Greek indices denote the coordinate directions  $x$  and  $y$ ). We derive the stiffness matrix  $\mathbf{K}^{\alpha\beta}$  for the planar modes to satisfy

$$K_{jk}^{xx} = \begin{cases} m_j \omega^2 + e\omega B^{\text{eff}}[j, \omega] - eV_0 + 2eV_{\omega} - k_e e^2 \sum_{l=1, l \neq j}^N \frac{(R_{jl}^0)^2 - 3(x_j^0 - x_l^0)^2}{(R_{jl}^0)^5}, & j = k \\ k_e e^2 \frac{(R_{jk}^0)^2 - 3(x_j^0 - x_k^0)^2}{(R_{jk}^0)^5}, & j \neq k, \end{cases}$$

$$\begin{aligned} K_{jk}^{yy} &= \begin{cases} m_j \omega^2 + e\omega B^{\text{eff}}[j, \omega] - eV_0 - 2eV_\omega - k_e e^2 \sum_{l=1, l \neq j}^N \frac{(R_{jl}^0)^2 - 3(y_j^0 - y_l^0)^2}{(R_{jl}^0)^5}, & j = k \\ k_e e^2 \frac{(R_{jk}^0)^2 - 3(y_j^0 - y_k^0)^2}{(R_{jk}^0)^5}, & j \neq k, \end{cases} \\ K_{jk}^{xy} &= \begin{cases} 3k_e e^2 \sum_{l=1, l \neq j}^N \frac{(x_j^0 - x_l^0)(y_j^0 - y_l^0)}{(R_{jl}^0)^5}, & j = k \\ -3k_e e^2 \frac{(x_j^0 - x_k^0)(y_j^0 - y_k^0)}{(R_{jk}^0)^5}, & j \neq k, \end{cases} \end{aligned} \quad (7)$$

where the equilibrium configuration is represented by the ion coordinates  $\mathbf{R}_j^0 = (x_j^0, y_j^0, z_j^0)$ , for  $j = 1, 2, \dots, N$ . Note that the off-diagonal matrix elements  $\mathbf{K}^{xy}$  have nonzero values, indicating the collective nature of the planar motional degrees of freedom, which couple the motion in the two coordinate directions together.

### B. Axial phonon modes

After applying the Euler-Lagrange equation to  $L_{\text{ph}}^A$  and substituting the eigenvector solution  $\delta R_j^z(t) = b_j^{zv} \cos[\omega_{zv}(t - t_0)]$ , we are left to solve the generalized eigenvalue equation,

$$\sum_{k=1}^N [\omega_{zv}^2 m_j \delta_{jk} - K_{jk}^{zz}] b_k^{zv} = 0, \quad v = 1, 2, \dots, N. \quad (8)$$

It is a simple procedure to convert this into a standard eigenvalue problem. First, we define the average mass to satisfy  $m_{\text{ave}} = \sum_{i=1}^N m_i / N$ . Then we define the mass matrix to be  $M_{jk} = m_j \delta_{jk}$ , which is a diagonal matrix. Finally, we define a new stiffness matrix via

$$\bar{\mathbf{K}}^{zz} = m_{\text{ave}} \mathbf{M}^{-\frac{1}{2}} \mathbf{K}^{zz} \mathbf{M}^{-\frac{1}{2}}, \quad (9)$$

which has the same physical units as the original stiffness matrix and remains real and symmetric. The inverse matrix square-root operation on the mass matrix  $\mathbf{M}$  is trivial to compute because the mass matrix is a diagonal matrix and all of its diagonal elements are positive, so  $M_{jk}^{-1/2} = \delta_{jk} / \sqrt{m_j}$ . We also define a new set of eigenvectors  $\bar{b}_j^{zv} = b_j^{zv} \sqrt{m_j} / \sqrt{m_{\text{ave}}}$  so that  $\bar{b}^{zv} = \mathbf{M}^{1/2} b^{zv} / \sqrt{m_{\text{ave}}}$ . These definitions now allow us to find a conventional eigenvalue problem to solve, namely,

$$\sum_{k=1}^N [m_{\text{ave}} \omega_{zv}^2 \delta_{jk} - \bar{K}_{jk}^{zz}] \bar{b}_k^{zv} = 0, \quad v = 1, 2, \dots, N. \quad (10)$$

Since the new stiffness matrix is real and symmetric, we can choose the eigenvectors to be real. Denoting the eigenvalues of  $\bar{\mathbf{K}}^{zz}$  by  $\lambda_{zv}$ , the eigenfrequencies for the axial modes become  $\omega_{zv} = \sqrt{\lambda_{zv}/m_{\text{ave}}}$ . The set of eigenvectors  $\{\bar{b}^{zv}, v = 1, \dots, N\}$  forms an orthonormal and complete set of eigenvectors because  $\bar{\mathbf{K}}^{zz}$  is a real and symmetric matrix. The original eigenvectors  $\{b^{zv} = \sqrt{m_{\text{ave}}} \mathbf{M}^{-1/2} \bar{b}^{zv}, v = 1, \dots, N\}$  will not, in general, be orthogonal, but instead they satisfy the following orthonormality conditions:

$$\sum_{j=1}^N \frac{m_j}{m_{\text{ave}}} b_j^{zv} b_j^{zv'} = \delta_{vv'}, \quad (11)$$

and the following completeness relation:

$$\sum_{v=1}^N b_j^{zv} b_k^{zv} = \frac{m_{\text{ave}}}{m_j} \delta_{jk}. \quad (12)$$

In Sec. III, we will show numerical results for the eigenvalue problem, but here we want to mention one important fact. When we have a pure system, all of the masses are identical, and one can immediately show that the center-of-mass mode involves an identical axial displacement of all of the ions, and hence it has a frequency equal to  $\omega_z$ . As defects are added into the system, the center-of-mass mode changes, with the heavier mass objects moving with a smaller amplitude. This then reduces the frequency of the mode, which is one of the simplest ways to determine that the crystal has defects (in fact, by tracking the discrete changes of this mode frequency, one can determine the precise number of defects at any given instant of time). See below in Fig. 7 where we show how the center-of-mass frequency tracks with the number of defects. Because the center-of-mass mode is no longer uniform, it will not generate a uniform spin-spin coupling between the different ions, which is possible only when the system has no defects.

The quantization condition is standard. We let  $\delta R_j^z(t) = \sum_v \xi_v(t) b_j^{zv} = \sum_v \xi_v(t) \bar{b}_j^{zv} \sqrt{m_{\text{ave}}/m_j}$  be the displacements from the equilibrium positions, with the quantum dynamics due to the  $v$ th phonon mode arising from the real generalized coordinate  $\xi_v(t)$ . The Lagrangian for the axial motion then becomes

$$L_{\text{ph}}^A = \frac{1}{2} \sum_{j=1}^N m_{\text{ave}} [\dot{\xi}_v^2 - \omega_{zv}^2 \xi_v^2]. \quad (13)$$

The generalized momentum is  $P_v^A = m_{\text{ave}} \dot{\xi}_v$ , and the Hamiltonian takes the standard form, which can be expressed as

$$H_{\text{ph}}^A = \sum_{v=1}^N \hbar \omega_{zv} \left( \hat{n}_{zv} + \frac{1}{2} \right), \quad (14)$$

where  $\hat{n}_{zv} = a_{zv}^\dagger a_{zv}$  is the phonon number operator, expressed in terms of the phonon raising and lowering operators, which satisfy

$$a_{zv}^\dagger = \sqrt{\frac{m_{\text{ave}} \omega_{zv}}{2\hbar}} \left( \xi_{zv} + \frac{i}{m_{\text{ave}} \omega_{zv}} P_v^A \right), \quad (15)$$

$$a_{zv} = \sqrt{\frac{m_{\text{ave}} \omega_{zv}}{2\hbar}} \left( \xi_{zv} - \frac{i}{m_{\text{ave}} \omega_{zv}} P_v^A \right). \quad (16)$$

The raising and lowering operators have the conventional commutation relations  $[a_{zv}, a_{zv'}^\dagger]_- = \delta_{vv'}$ . The axial displacement is

then represented as an operator in the following two equivalent forms:

$$\begin{aligned}\delta\hat{R}_j^z &= \sum_v \sqrt{\frac{\hbar}{2m_{\text{ave}}\omega_{zv}}} (a_{zv}^\dagger + a_{zv}) b_j^{zv} \\ &= \sum_v \sqrt{\frac{\hbar}{2m_j\omega_{zv}}} (a_{zv}^\dagger + a_{zv}) \bar{b}_j^{zv}.\end{aligned}$$

Finally, we need to derive the effective spin-spin interactions that arise when an optical dipole force is applied to the system in the axial direction. The analysis is identical to that given before [12,17], with the mass replaced by the average mass, due to the form of the expansion of the coordinate in terms of the phonon raising and lowering operators and the  $b^{zv}$  generalized eigenvectors. Hence, we find that the Ising spin-spin coupling between sites  $j$  and  $j'$  is

$$\begin{aligned}J_{jj'}(t) &= \frac{F_O^2}{4m_{\text{ave}}} \sum_{v=1}^N \frac{b_j^{zv} b_{j'}^{zv}}{\mu^2 - \omega_{zv}^2} \\ &\times \left[ 1 + \cos 2\mu t - \frac{2\mu}{\omega_{zv}} \sin \omega_{zv} t \sin \mu t \right],\end{aligned}\quad (17)$$

where  $F_O$  is the magnitude of the optical dipole force, and  $\mu$  is the beat-note frequency corresponding to the frequency difference of the two off-resonant laser beams being applied to the trapped ion crystal. The symbol  $\mu$  is also referred to as the detuning of the optical dipole force from the phonon modes, since the crystal is resonantly driven when the beat-note frequency (or detuning) is equal to a normal-mode frequency  $\omega_{zv}$ . Of course, the spin-spin interactions only hold between the pure atomic species, since the energy levels and matrix elements change for the defect sites, so the sites  $j$  and  $j'$  must both be sites without defects in order for there to be a spin-spin interaction generated by the optical dipole force.

### C. Planar phonon modes

Now we discuss the planar phonon modes, which are more complicated. Applying the Euler-Lagrange equations to the classical planar Lagrangian  $L_{\text{ph}}^P$  results in the following coupled equations of motion in the  $xy$  plane:

$$\begin{aligned}m_j \delta \ddot{R}_j^x + \sum_{k=1}^N [K_{jk}^{xx} \delta R_k^x + K_{jk}^{xy} \delta R_k^y - e B_{\text{eff}}[j, \omega] \delta_{jk} \delta \dot{R}_k^y] \\ = 0, \\ m_j \delta \ddot{R}_j^y + \sum_{k=1}^N [K_{jk}^{yy} \delta R_k^y + K_{jk}^{yx} \delta R_k^x + e B_{\text{eff}}[j, \omega] \delta_{jk} \delta \dot{R}_k^x] \\ = 0,\end{aligned}\quad (18)$$

where the ion index  $j$  runs from 1 to  $N$ . We assume that we have a set of  $2N$  planar eigenfrequencies  $\omega_\lambda$  and we express the displacements at each site in terms of “composite” eigenvectors  $\sum_{v=1}^{2N} \alpha_\lambda^v b_j^{av}$ , where  $\alpha_\lambda^v$  are complex eigenvectors, while  $b_j^{av}$  are real eigenvectors, described below. The superscript  $a$  denotes the  $x$  or  $y$  spatial components. Hence, we let

$$\delta R_j^a(t) = \sum_{\lambda=1}^{2N} \sum_{v=1}^{2N} \frac{1}{2} [\alpha_\lambda^{av*} e^{i\omega_\lambda t} + \alpha_\lambda^v e^{-i\omega_\lambda t}] b_j^{av}\quad (19)$$

$$= \sum_{\lambda=1}^{4N} \sum_{v=1}^{2N} \frac{1}{2} \text{Re}[\alpha_\lambda^v e^{-i\omega_\lambda t}] b_j^{av},\quad (20)$$

where the eigenvectors denoted by  $\lambda$  appear in pairs for which the complex conjugate has a negative eigenvalue  $-\omega_\lambda$ ; the eigenvectors and eigenvalues are ordered so the first  $2N$  have positive eigenvalues and the latter  $2N$  have negative eigenvalues. The substitution of this final expression into the equations of motion yields the following quadratic eigenvalue problem:

$$[\mathbf{M}\omega_\lambda^2 + i\omega_\lambda \mathbf{T} - \mathbf{K}] \mathbf{Q}^\lambda = 0, \quad \lambda = 1, 2, \dots, 2N,\quad (21)$$

in which  $\mathbf{M}$  is the diagonal mass matrix with  $M_{i\alpha,j\beta} = m_j \delta_{ij} \delta_{\alpha\beta}$ ,  $\mathbf{T}$  is a real antisymmetric matrix defined by  $T_{i\alpha,j\beta} = -e B_{\text{eff}}(j, \omega) \delta_{ij} \epsilon_{\alpha\beta}$  with  $\epsilon_{xy} = -\epsilon_{yx} = 1$  (and all other choices vanish),  $\mathbf{K}$  is the (real symmetric) stiffness matrix in the  $xy$  plane given by

$$\mathbf{K} = \begin{pmatrix} \mathbf{K}^{xx} & \mathbf{K}^{xy} \\ \mathbf{K}^{yx} & \mathbf{K}^{yy} \end{pmatrix},\quad (22)$$

and the column eigenvector  $\mathbf{Q}^\lambda$  satisfies  $Q_{i\alpha}^\lambda = \sum_v \alpha_\lambda^v b_i^{av}$ . In all cases, we are using a double index to represent the  $2N \times 2N$  matrices, with  $i$  running over indices  $1, \dots, N$ , first with  $\alpha = x$  and then with  $\alpha = y$ . We also assume that we are considering only the eigenvectors corresponding to non-negative eigenvalues,  $\omega_\lambda \geq 0$ .

We begin our analysis by defining a new set of matrices  $\bar{\mathbf{T}} = m_{\text{ave}} \mathbf{M}^{-1/2} \mathbf{T} \mathbf{M}^{-1/2}$  and  $\bar{\mathbf{K}} = m_{\text{ave}} \mathbf{M}^{-1/2} \mathbf{K} \mathbf{M}^{-1/2}$ , and a new vector  $\bar{b}^{av} = \mathbf{M}^{1/2} b^{av} / \sqrt{m_{\text{ave}}}$ . The quadratic eigenvalue problem then becomes

$$[m_{\text{ave}} \omega_\lambda^2 \mathbb{I} + i\omega_\lambda \bar{\mathbf{T}} - \bar{\mathbf{K}}] \bar{\mathbf{Q}}^\lambda = 0, \quad \lambda = 1, \dots, 2N,\quad (23)$$

where  $\bar{Q}_{i\alpha}^\lambda = \sum_v \alpha_\lambda^v b_i^{av} \sqrt{m_i/m_{\text{ave}}}$  is the  $\lambda$ th eigenvector and all eigenvalues  $\omega_\lambda$  remain non-negative. Next, we define the real orthonormal eigenvectors  $\bar{b}^{av}$  to satisfy

$$\sum_{j\beta} \bar{\mathbf{K}}_{i\alpha,j\beta} \bar{b}_j^{bv} = m_{\text{ave}} (\omega_0^v)^2 \bar{b}_i^{av}, \quad v = 1, 2, \dots, 2N,\quad (24)$$

where  $\omega_0^v \geq 0$  is the normal-mode frequency for motion in a vanishing effective magnetic field. Then, we form the matrix  $\bar{\mathbf{B}}$  from the column vectors  $\bar{b}^v$  and we evaluate the quadratic eigenvalue problem in the basis of the eigenvectors of  $\bar{b}^v$  by multiplying on the left by  $\bar{\mathbf{B}}^{-1} = \bar{\mathbf{B}}^T$  and inserting  $\mathbb{I} = \bar{\mathbf{B}} \bar{\mathbf{B}}^{-1}$  before the vector  $\bar{\mathbf{Q}}$ . This gives

$$[m_{\text{ave}} \omega_\lambda^2 \mathbb{I} + i\omega_\lambda \bar{\mathbf{T}} - \bar{\mathbf{K}}] \bar{\mathbf{Q}}^\lambda = 0, \quad \lambda = 1, 2, \dots, 2N,\quad (25)$$

with  $\bar{\mathbf{T}} = \bar{\mathbf{B}}^T \bar{\mathbf{T}} \bar{\mathbf{B}}$ ,  $\bar{\mathbf{K}}_{vv'} = m_{\text{ave}} (\omega_0^v)^2 \delta_{vv'}$ , and  $\bar{\mathbf{Q}} = \bar{\mathbf{B}}^T \bar{\mathbf{Q}}$ . Since these matrices are in the basis of the eigenvectors of  $\bar{\mathbf{K}}$ , they use the eigenvector index  $v$  for the components of the stiffness matrix, which is diagonal, of course. In addition, using the orthonormality of the  $\bar{b}$  eigenvectors, one immediately sees that  $\bar{Q}_v^\lambda = \alpha_\lambda^v$ .

The eigenvalues of the quadratic eigenvalue problem are all real, and by taking the complex conjugate of Eq. (25), it is easy to see that if  $\omega_\lambda$  is the eigenvalue corresponding to the eigenvector  $\alpha_\lambda$ , then  $-\omega_\lambda$  is the eigenvalue corresponding to  $\alpha_\lambda^*$ . Since the solution of a nontrivial quadratic eigenvalue problem is not obvious, we map it onto a conventional

eigenvalue problem by doubling the size of the matrices. We do so in a symmetrized fashion, so that the resulting matrix is Hermitian (but complex), and the solution of the eigenvalue problem follows conventional linear algebra techniques. The associated linear eigenvalue problem is

$$\begin{pmatrix} -i\bar{\mathbf{T}}/m_{\text{ave}} & (\bar{\mathbf{K}}/m_{\text{ave}})^{1/2} \\ (\bar{\mathbf{K}}/m_{\text{ave}})^{1/2} & 0 \end{pmatrix} \times \begin{pmatrix} \omega_\lambda \alpha_\lambda \\ (\bar{\mathbf{K}}/m_{\text{ave}})^{1/2} \alpha_\lambda \end{pmatrix} = \omega_\lambda \begin{pmatrix} \omega_\lambda \alpha_\lambda \\ (\bar{\mathbf{K}}/m_{\text{ave}})^{1/2} \alpha_\lambda \end{pmatrix}, \quad (26)$$

where  $([\bar{\mathbf{K}}/m_{\text{ave}}]^{1/2} \alpha_\lambda)_v = \omega_0^\nu \alpha_\lambda^\nu$ , since the stiffness matrix is diagonal in this basis (the repeated  $\nu$  does *not* imply a summation over  $\nu$ ). It is straightforward to show that the solution of this linear eigenvalue problem solves the original quadratic eigenvalue problem. We organize the solutions so that the first  $2N$  eigenvalues are positive and the second  $2N$  eigenvalues are negative. Since the negative eigenvectors of the quadratic eigenvalue problem are related to the positive eigenvectors via complex conjugation, we automatically know the negative eigenvectors once the positives are known. Note that working in the  $\bar{b}$  basis produces a diagonal form for the spring-constant matrix, which allows us to easily take the matrix square root.

The eigenvectors of the linear eigenvalue problem (of dimension  $4N$ ) satisfy the conventional orthogonality and completeness relations of Hermitian eigenvalue problems, but we choose them not to be normalized so that we can find more standard relations between the  $\alpha_\lambda$  eigenvectors. Following the approach of Refs. [12,18], one can derive the following relations based on orthogonality and completeness:

$$\sum_{\nu=1}^{2N} (\omega_\lambda \omega_{\lambda'} + \omega_0^{\nu 2}) \alpha_\lambda^{\nu *} \alpha_{\lambda'}^\nu = \frac{\omega_\lambda}{\hbar m_{\text{ave}}} \delta_{\nu\nu'}, \quad (27)$$

$$\sum_{\lambda: \omega_\lambda > 0} \omega_\lambda (\alpha_\lambda^{\nu *} \alpha_{\lambda'}^\nu + \alpha_\lambda^\nu \alpha_{\lambda'}^{\nu *}) = \frac{1}{\hbar m_{\text{ave}}} \delta_{\nu\nu'}, \quad (28)$$

$$\sum_{\lambda: \omega_\lambda > 0} (\alpha_\lambda^{\nu *} \alpha_{\lambda'}^\nu - \alpha_\lambda^\nu \alpha_{\lambda'}^{\nu *}) = 0, \quad (29)$$

$$\sum_{\lambda: \omega_\lambda > 0} \frac{1}{\omega_\lambda} (\alpha_\lambda^{\nu *} \alpha_{\lambda'}^\nu + \alpha_\lambda^\nu \alpha_{\lambda'}^{\nu *}) = \frac{1}{\hbar m_{\text{ave}} \omega_0^{\nu 2}} \delta_{\nu\nu'}, \quad (30)$$

which corrects a typo in Eq. (A5) of Ref. [12]. In the last three of these expressions, the second terms in the parentheses arise from the negative eigenvalue solutions of the quadratic eigenvalue problem.

The quantization procedure for the planar modes is also nonstandard [12,18]. The complications arise because the generalized momentum operators do not commute with each other due to the magnetic field. The procedure to properly quantize the Hamiltonian is still fairly standard, and we present only a sketch of the full derivation here. We begin with the definition of the generalized coordinate that we will be using. We let the displacement be represented by

$$\delta R_j^\alpha(t) = \sum_{\nu=1}^{2N} \zeta_\nu(t) b_j^{\alpha\nu} \quad (31)$$

$$= \sum_{\nu=1}^{2N} \zeta_\nu(t) \bar{b}_j^{\alpha\nu} \sqrt{\frac{m_{\text{ave}}}{m_j}}, \quad (32)$$

where  $\zeta_\nu$  is the generalized coordinate for  $1 \leq \nu \leq 2N$ . As discussed above, the eigenvectors  $b$  or  $\bar{b}$  are both real, so the displacement is real. The mechanical momentum satisfies  $\Pi^\nu = m_{\text{ave}} \dot{\zeta}_\nu(t)$ . The corresponding generalized momentum is

$$P^\nu = \Pi^\nu - \frac{1}{2} \sum_{\nu'} \zeta_{\nu'} \bar{T}_{\nu'\nu}, \quad (33)$$

where  $\bar{T}$  is the antisymmetric matrix that represents the effective magnetic field in the basis of the  $\bar{b}$  eigenvectors, as described above. The classical Hamiltonian now takes a simple form in terms of the mechanical momentum and the generalized coordinate:

$$H_{\text{ph}}^P = \frac{1}{2m_{\text{ave}}} \sum_\nu (\Pi^\nu)^2 + \frac{1}{2} m_{\text{ave}} \sum_\nu (\omega_0^\nu)^2 (\zeta_\nu)^2. \quad (34)$$

The problem with quantization is that we quantize with respect to the generalized momentum, not the mechanical momentum, so the mechanical momentum commutation relation becomes nonzero between different spatial directions. In other words, we take conventional commutation relations, where the  $\hat{\zeta}$  operators commute with themselves, as do the  $\hat{P}$  operators, and we take  $[\hat{\zeta}_\nu, \hat{P}^{\nu'}]_- = i\hbar \delta_{\nu\nu'}$ . Then,  $[\hat{\Pi}^\nu, \hat{\Pi}^{\nu'}]_- = -i\hbar \bar{T}_{\nu\nu'}$ . To complete the quantization, we construct the raising and lowering operators in terms of nonstandard combinations of the coordinate and mechanical momentum operators,

$$\hat{a}_\lambda^\dagger = \sum_{\nu=1}^{2N} \left[ \alpha_\lambda^\nu \Pi^\nu + im_{\text{ave}} \frac{(\omega_0^\nu)^2}{\omega_\lambda} \alpha_\lambda^\nu \zeta_\nu \right], \quad (35)$$

$$\hat{a}_\lambda = \sum_{\nu=1}^{2N} \left[ \alpha_\lambda^{\nu *} \Pi^\nu - im_{\text{ave}} \frac{(\omega_0^\nu)^2}{\omega_\lambda} \alpha_\lambda^{\nu *} \zeta_\nu \right]. \quad (36)$$

Using the relations satisfied by the  $\alpha_\lambda$  eigenvectors, one can immediately verify that  $[\hat{a}_\lambda, \hat{a}_{\lambda'}^\dagger]_- = \delta_{\lambda\lambda'}$  (and the commutators of two  $\hat{a}$ 's or two  $\hat{a}^\dagger$ 's vanish). The quantized Hamiltonian then takes the standard form

$$\hat{H}_{\text{ph}}^P = \sum_{\lambda=1}^{2N} \hbar \omega_\lambda \left( \hat{a}_\lambda^\dagger \hat{a}_\lambda + \frac{1}{2} \right), \quad (37)$$

which can be directly verified by substitution or by checking that  $[\hat{H}_{\text{ph}}^P, \hat{a}_\lambda^\dagger]_- = \hbar \omega_\lambda \hat{a}_\lambda^\dagger$ . Finally, the expression for the coordinate in terms of the raising and lowering operators becomes

$$\hat{\zeta}_\nu = -i\hbar \sum_{\lambda: \omega_\lambda > 0} (\alpha_\lambda^{\nu *} \hat{a}_\lambda^\dagger - \alpha_\lambda^\nu \hat{a}_\lambda). \quad (38)$$

This relation is needed as the starting point to determine the effective spin-spin interactions, as it is needed to be substituted into the optical dipole force Hamiltonian which couples the spins to the positions of the ions [12,17].

Since there are a number of different ways that one might invoke an effective spin-spin coupling that employs driving the planar phonon modes, but none have been implemented experimentally yet, we do not examine effective spin-spin interactions in the planar directions any further in this work. Of course, it would be a straightforward procedure to go from

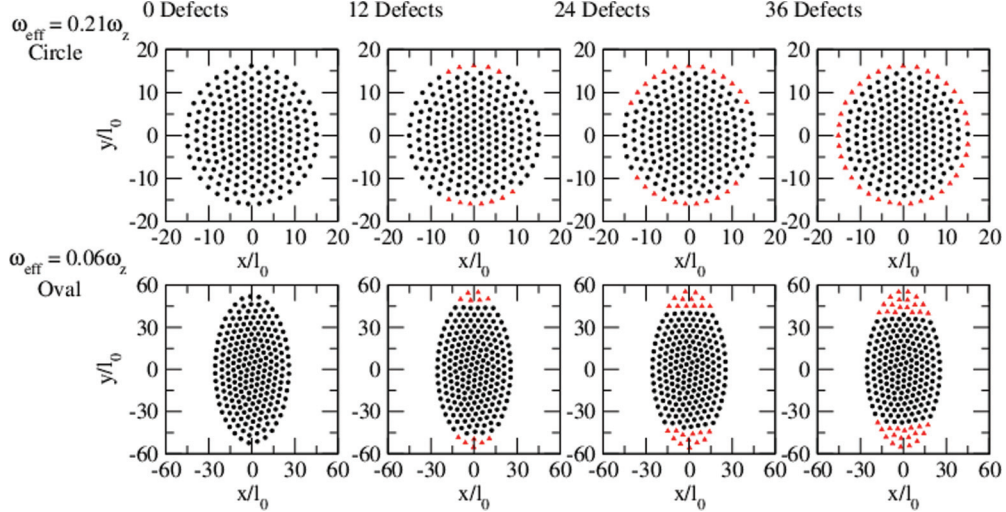


FIG. 2. (Color online) Equilibrium structures for  $N = 217$  ions and a weak wall ( $\omega_W = 0.04\omega_z$ ) with different rotating frequencies. The top panels are the faster rotating circular case and the bottom panels the slower rotating oval case. The panels show  $N_d = 0, 12, 24$ , and  $36$ . Black circles denote  $\text{Be}^+$  ions and red triangles denote  $\text{BeH}^+$  molecules. Note the difference in the spatial scales for the upper and lower panels.

the quantized phonons to the spin-spin interactions when a spin-dependent force is applied, and this can be done in the future if it is needed for the case with defects in the ion crystal.

### III. NUMERICAL RESULTS

We present several numerical examples to illustrate the effect of defects on the equilibrium structure, eigenvalues, and eigenvectors of the normal modes, and the spin-spin interaction  $J_{ij}$  for the axial modes detuning above the center-of-mass mode. As in previous work, we use the axial center-of-mass phonon frequency (for the pure case)  $\omega_z = 2\pi \times 795$  kHz (in units of rad/s) as the angular frequency unit. We define  $\omega_W = \sqrt{2e|V_W|/m_{\text{Be}^+}}$  and only consider the weak wall case,  $\omega_W = 0.04\omega_z$ . We use the beryllium ion mass of  $m_{\text{Be}^+} = 9.012182u$  and  $\text{BeH}^+$  ion mass of  $m_{\text{BeH}^+} = 10.0201220u$ , where  $u$  is the atomic mass unit. The magnitude of the magnetic field is  $B_z = 4.5$  T corresponding to a cyclotron frequency  $\omega_c(\text{Be}^+) = eB_z/m_{\text{Be}^+} = 9.645\omega_z$  for the beryllium ions and  $\omega_c(\text{BeH}^+) = eB_z/m_{\text{BeH}^+} = 8.675\omega_z$  for beryllium hydride ions. We define the effective trapping frequency in the plane as  $\omega_{\text{eff}} = \sqrt{\omega_c\omega - \omega^2 - eV_0/m_{\text{Be}^+}}$  and only consider the effective frequencies  $\omega_h = 0.21\omega_z$  (rotation frequency  $\omega = 2\pi \times 45.3$  kHz for  $\omega_z = 2\pi \times 795$  kHz) and  $\omega_l = 0.06\omega_z$  (rotation frequency  $\omega = 2\pi \times 41.3$  kHz for  $\omega_z = 2\pi \times 795$  kHz). We work with an ion crystal that has a total of  $N = 217$  particles and allow it to have up to  $N_d = 36$  defects.

#### A. Equilibrium configurations

In Fig. 2, we plot the equilibrium positions of the ions when the system has a number of defects added for the two different rotation rates for the rotating wall potential. One is a faster rotation rate, which tends to have closer-packed circular-shaped crystals, and the other is a slower rotation, which has a much larger-sized crystal with a marked oval

asymmetry. Note how, in the circular case, the defects occupy the outer ring of the structure, while in the oval case, they are pushed primarily to the tips of the oval. Note how the spatial scale is three times larger in the bottom row (oval case). In general, while the equilibrium positions are certainly changed when defects are added, the change is not too large and affects primarily the defect sites.

#### B. Normal modes

There are three branches of phonon modes. The planar modes are described by the low-energy magnetron modes and the high-energy cyclotron modes. The magnetron mode eigenvalues are hardly changed by the presence of defects, so we do not replot their values here. The cyclotron modes have very little dispersion and are centered around the different cyclotron frequencies, hence  $N_d$  of the eigenvalues are near  $\omega_c(\text{BeH}^+)$  and  $N - N_d$  eigenvalues are near  $\omega_c(\text{Be}^+)$ . We show details of this behavior below, but first we show the eigenvalues for the axial mode frequencies, which can have large dispersion and have a more complicated dependence on the number of defects.

The axial eigenvalues are plotted in Fig. 3 for the pure case and the case with  $N_d = 36$  defects. All modes clearly show an overall suppression of the phonon frequencies, while approximately  $N_d$  of the modes are being suppressed by a larger amount (on the order of 3%), which might be expected due to the mass difference. What is perhaps more surprising is that the  $N_d$  modes that are suppressed more than the average ones occur at different regions of the spectrum when the shape of the equilibrium crystal changes. In the circular case, they lie near the top of the spectrum and, in the oval case, they lie near the bottom. The most probable explanation is that the isolated clustering of the defects in the oval case lends that system to have more localized modes that primarily involve the motion of defects only or of  $\text{Be}^+$  ions only, which then shifts the lower-energy frequencies due to the defects since the center-of-mass mode is the highest-frequency mode for

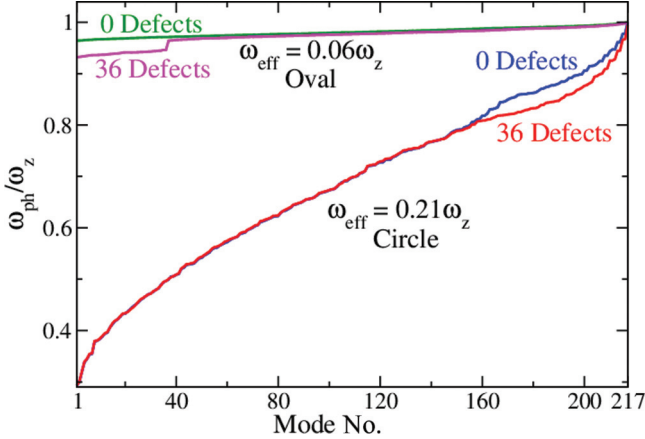


FIG. 3. (Color online) Eigenfrequencies of the axial modes with defects for the fast and slow rotating cases. In general, there are about  $N_d$  modes that are changed due to the defects, and these tend to be at the higher frequencies for the faster rotating case with a more circular profile and closer to the lower frequencies for the slower rotating oval case. The modes are plotted vs mode number, sorted according to increasing phonon frequencies.

the axial phonons. This effect is much reduced for the more circular crystals, where the defects are more evenly positioned around the perimeter of the crystal and the crystal is more homogeneous and closely packed, so that the largest change is for the collective modes that involve the motion of all ions and lie near the top of the spectrum.

A false color schematic of the four highest eigenvectors is plotted in Fig. 4. One can see that the eigenvectors do not have significant change for these four cases, although the center-of-mass mode is clearly no longer uniform. Cases that have more complex behavior do appear in the eigenvectors. In Fig. 5, we can see some cases of this behavior. In the top panel, we show how one of the modes for the defect case for fast rotation is almost exactly related to a linear combination of two nearby modes in the pure system, while for the defect case for slow rotation, in the lower panel, we can see that one of the defect modes is (roughly) related to a linear combination of two nearby pure modes.

The fact that different phonon modes in the pure case are approximately combined into new modes for the defect case can be studied more quantitatively by determining the overlap of the defect eigenvectors onto the eigenvectors for the pure case. This is done by computing the normalized ( $\bar{b}$ ) eigenvectors for the relative displacements of the pure system, taking the dot product with the defect-case eigenvectors and taking the absolute value. We use the  $\bar{b}$  eigenmodes because they form two orthonormal sets of vectors, so the expression is

$$\text{Projection on } v\text{th mode} = \left| \sum_i \bar{b}_i^{zv} (N_d = 36) \bar{b}_i^{zv} (N_d = 0) \right|. \quad (39)$$

We plot these results as a function of the mode numbers (sorted according to increasing phonon frequency) in Fig. 6 with a false color image. The fact that the results for the circular case (top) lie predominantly on the diagonal indicates that the

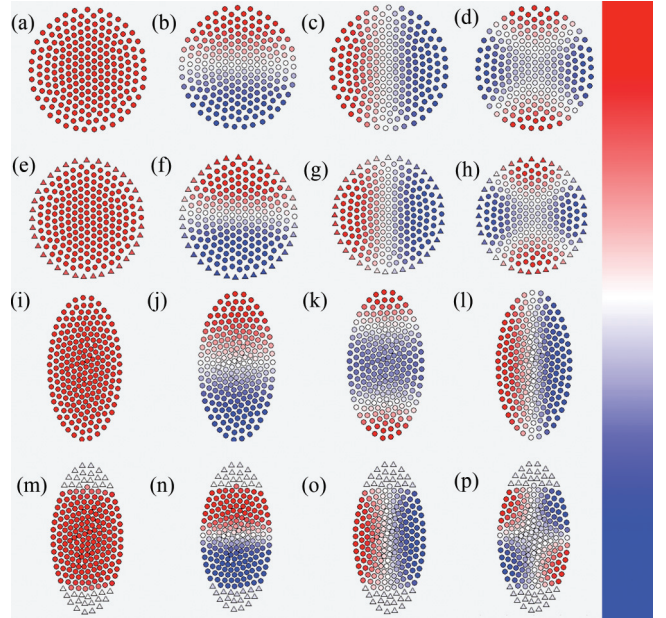


FIG. 4. (Color online) False color image of the first four eigenvectors for the pure (top) and  $N_d = 36$  defect (bottom) case for the (a)–(h) fast rotating and (i)–(p) slow rotating cases. Note how the eigenvectors are quite similar for the cases without [upper, (a)–(d); (i)–(l)] and with [lower, (e)–(h); (m)–(p)] defects. Be<sup>+</sup> ions are plotted with circles; BeH<sup>+</sup> defects are plotted with triangles. A careful inspection shows that the center-of-mass mode (far left) is no longer uniform for the defect case. Note that the defects can also change the ordering of the eigenvectors when sorted according to their eigenvalues, as seen by comparing panels (j)–(l) with (n)–(p). The color scale for the false color image is on the right.

character of the modes does not change so much as the defects are added, but the effect becomes more severe near the higher

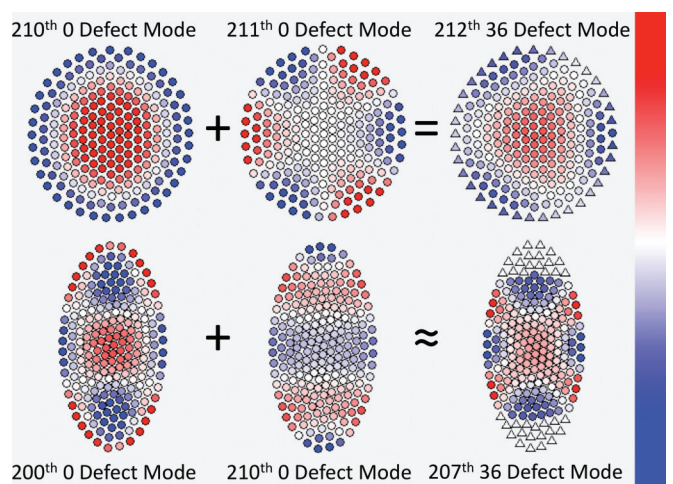


FIG. 5. (Color online) False color image showing how one of the defect modes is related to simple linear combinations of different pure modes with similar eigenvalues. The top panel is for the fast rotating circular case where a sum of the two pure case modes is essentially equal to the defect mode and the bottom panel is for the slower rotating oval case where the sum of the two modes is approximately equal to the defect mode.

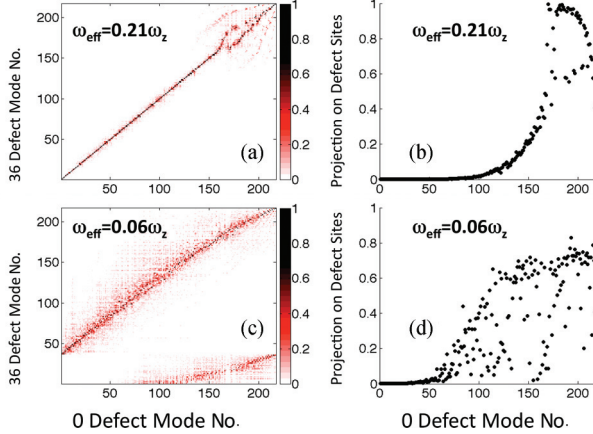


FIG. 6. (Color online) False color image of the dot product of the pure-case eigenmodes with the corresponding defect-case eigenmodes (left) and norm of the pure-case eigenmode restricted to the defect sites (right). Two cases are shown: (i) fast rotation (circular) case on the top and (ii) slow rotation (oval) case on the bottom.

modes, and this is precisely where the phonon frequencies were changed the most in the system. For the oval case (bottom), we see two high weight tracks and significantly more spread among the results. This indicates that the defects are having a much more significant effect on the eigenvectors, but the second track on the subdiagonal indicates that the main effect is a reordering of the numbers of the modes, arising primarily from the phonons being more localized on the defect-free and defect regions separately. In the right panels, we project the motion of the eigenvectors for the pure case onto the positions of the defects. This is done by first determining the  $N_d = 36$  positions for the equilibrium configuration that are farthest from the origin. We project the pure-case eigenvector onto those defect sites and compute the norm of the projected vector. This norm is called the projection of the pure eigenmode onto the defect sites and is plotted in the right panels. One can

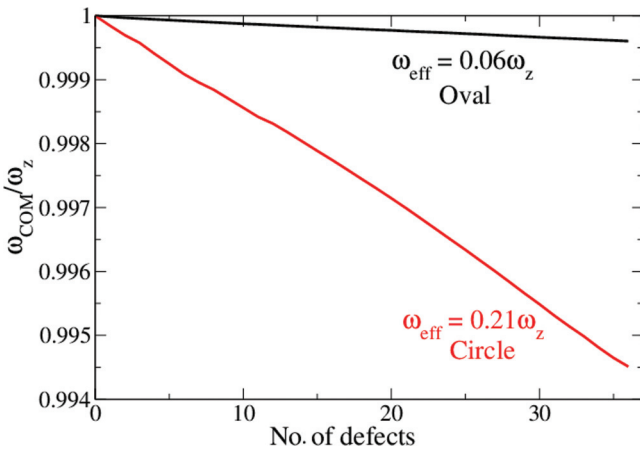


FIG. 7. (Color online) Axial center-of-mass frequency as a function of the number of defects for the fast (black curve) and slow (red curve) cases. One can use these curves along with the measurement of the center-of-mass frequency to determine the number of defects in the system at any given moment of time (assuming the defects rapidly move to the boundary due to centrifugal effects).

see that there are far more modes with projections onto the defect sites for the oval case than for the circular case, and this explains why the eigenmodes have more mixing of the pure-case modes in the oval case. Modes with little mixing on the defect sites will not have their frequencies changed by too much. These tend to be the low-mode-number localized modes of the axial eigenvectors.

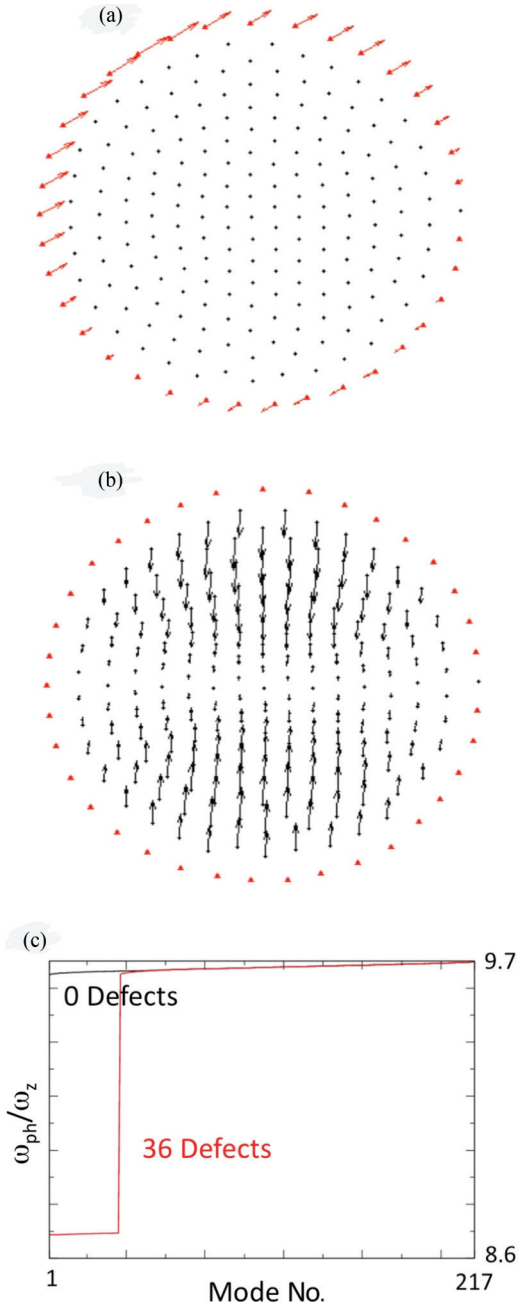


FIG. 8. (Color online) Visualization of some example cyclotron modes (a) and (b) and of the mode spectrum (c) for  $N_d = 36$  and the fast rotating case; arrows indicate the instantaneous motion of the respective ionic site. One can see that the cyclotron modes separate into motion (a) of the defects only or (b) of the  $\text{Be}^+$  only. The mode spectrum is shown in (c), where one can clearly see the separation of the motion according to the two different cyclotron frequencies for the defect case.

We next show how the center-of-mass mode changes with the number of defects for the two cases of fast and slow rotation in Fig. 7. These curves are fairly linear, although structures in them can be clearly seen. The slopes depend strongly on the shape of the crystal, being much smaller for the oval case. The relative shift of the frequency is small because the mass difference is only of the order of 10% between the pure and defect sites.

We end this section by plotting some properties of the cyclotron planar modes in Fig. 8. Figures 8(a) and 8(b) show two selected modes of motion. One can see that these modes are separated into motion of the defects only or motion of the  $\text{Be}^+$  ions only, with very little coherent motion between the two species. This occurs because the cyclotron motions of the two species are so different, much more so than the dispersion of the modes, and hence there is little collective motion between the two species. Example movies of these phonon modes are shown in the Supplemental Material [19].

### C. Ising spin-spin interaction for an axial drive

Now that we have described how defects alter the phonon properties, we investigate how the spin-spin interactions compare to the pure case. By coupling the phonons to the spins with a spin-dependent optical force, one can generate an Ising Hamiltonian ( $\sigma_i^z$  is the Pauli spin matrix in the  $z$  direction

at site  $i$ ),

$$\mathcal{H} = \sum_{ij} J_{ij} \sigma_i^z \sigma_j^z, \quad (40)$$

where we have neglected time-dependent terms, and the sum is only over pure sites where a  $\text{Be}^+$  ion lies. This is because as defects are added to the system, those sites no longer have an addressable spin, and hence we only compute the spin-spin interactions between two sites that each contain a  $\text{Be}^+$  ion. Hence the spin-spin couplings become

$$J_{ij} = \frac{F_0^2}{4m_{\text{ave}}} \sum_{v=1}^N \frac{b_i^{zv} b_j^{zv}}{\mu^2 - \omega_{zv}^2}, \quad (41)$$

for  $i$  and  $j$   $\text{Be}^+$  sites only.

To be specific, we examine detuning to the blue of the center-of-mass mode, correcting the detuning to lie to the blue of the center-of-mass mode with the defects. This way, all of the results will be compared on an equal footing. Since the spin-spin couplings should behave like a power law in the distance between the ions, we fit the tails of the distributions to power laws. The full range of the power-law behavior ranges from 0 to 3, but because the center-of-mass mode is nonuniform when defects are present, the power law will not extend all the way down to zero.

Results are shown in Fig. 9 for the faster rotating circular crystal. One can immediately see that the main effect of the defects is to slightly increase the power law for an equivalent detuning, and for there to be a larger spread to the data as a

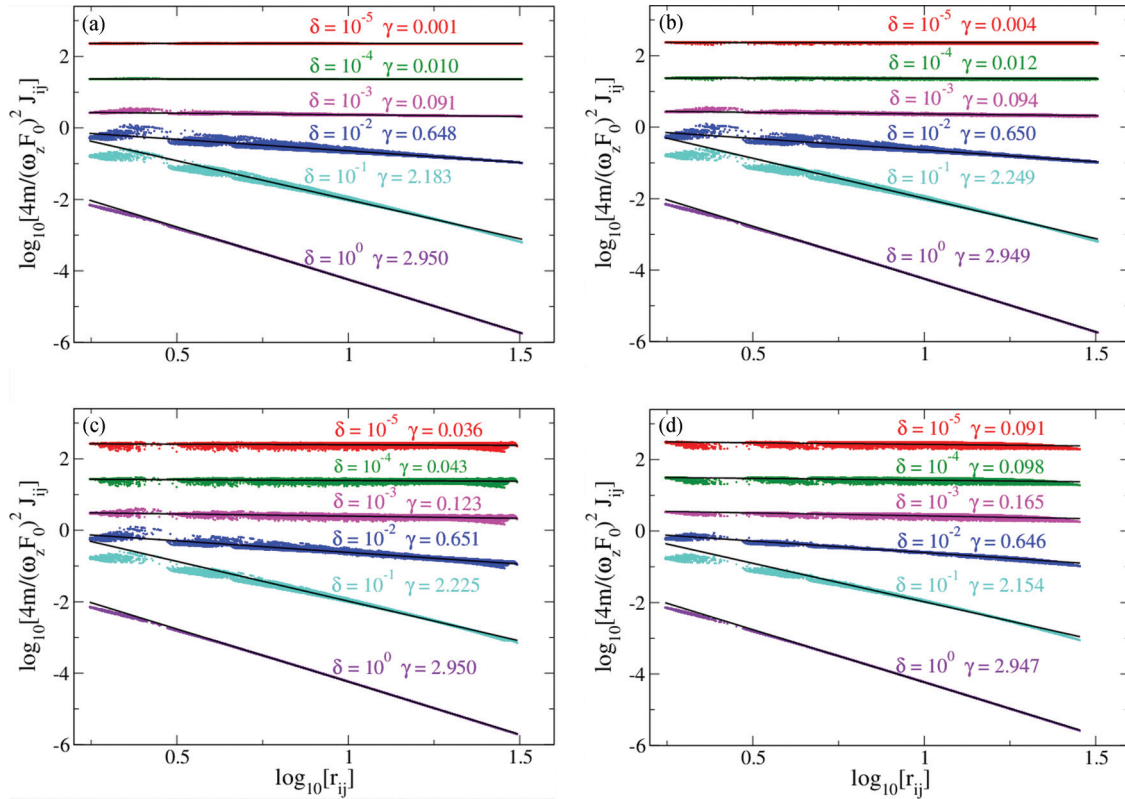


FIG. 9. (Color online) Spin-spin couplings vs distance for different detunings (different colored lines) and different number of defects [(a) 0, (b) 1, (c) 18, and (d) 36 defects] on a log-log plot. The straight-line fits show power-law behavior  $J_{ij} \propto r_{ij}^{-\gamma}$ . The detunings are  $\mu = \omega_{\text{cm}} + \delta\omega_z$ , with  $\delta = 10^{-5}, 10^{-4}, 10^{-3}, 10^{-2}, 10^{-1}$  and 1. This case is for the faster rotating circular crystal.

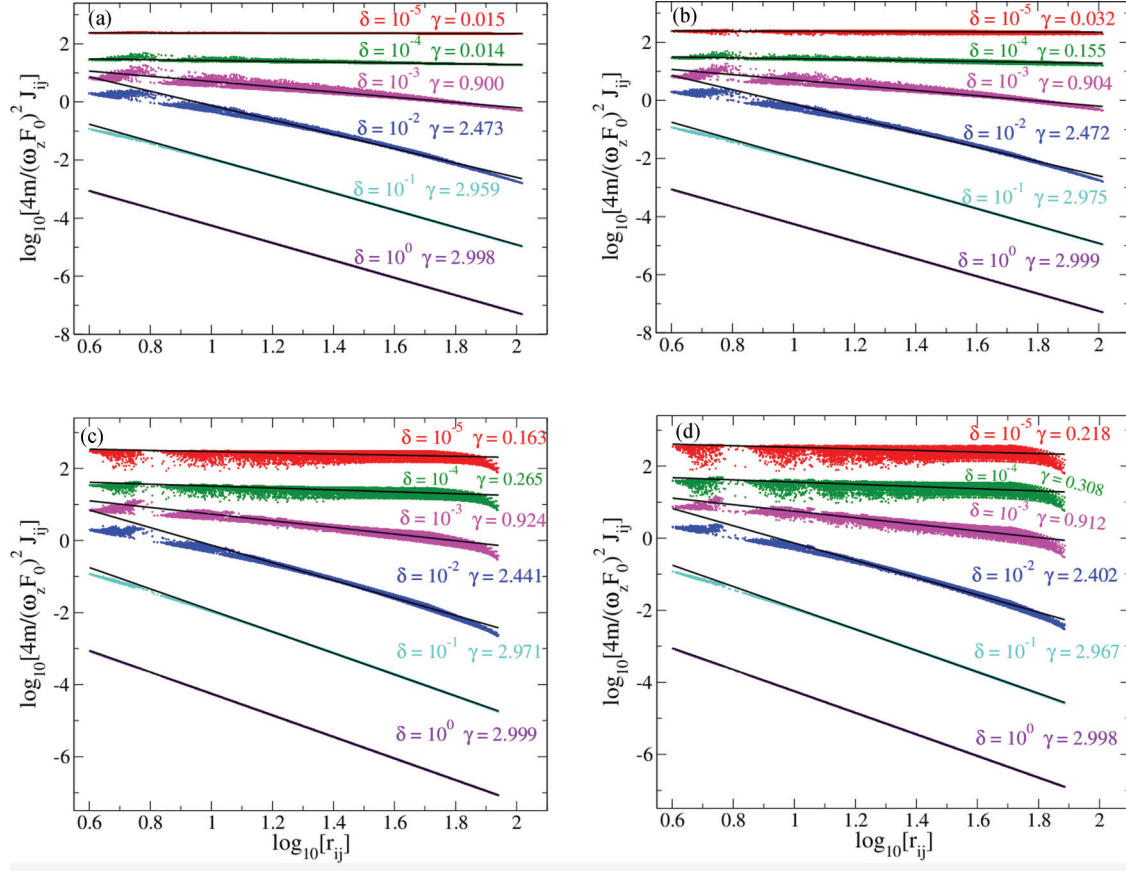


FIG. 10. (Color online) Spin-spin couplings vs distance for different detunings (different colored lines) and different number of defects [(a) 0, (b) 1, (c) 18, and (d) 36 defects] on a log-log plot. The straight-line fits show power-law behavior  $J_{ij} \propto r_{ij}^{-\gamma}$ . The detunings are  $\mu = \omega_{cm} + \delta\omega_z$ , with  $\delta = 10^{-5}, 10^{-4}, 10^{-3}, 10^{-2}, 10^{-1}$  and 1. This case is for the slower rotating oval-shaped crystal.

function of distance when there are more defects. In particular, when there are enough defects, it is difficult to get to the point where the power law approaches zero. These results are quite important for experiment, as they show that the defects do not significantly alter the behavior of the spin-spin interactions, and hence one does not need to maintain perfect purity when running a given experiment. The only issue that arises is that one needs to ensure the detuning remains fixed relative to the center-of-mass mode by keeping the number  $\delta$  constant during the experiment [ $\mu = \omega_{cm} + \delta\omega_z$ ], which does require carefully monitoring the center-of-mass mode frequency. Not doing so will give rise to a somewhat larger drift of the power laws as more defects are added to the crystal.

The situation is a bit different for the slower rotating oval crystal, depicted in Fig. 10. Here, as the number of defects rises, we see two effects. The first is an overall broadening of the width of the distribution of the couplings, especially for cases where the detuning is close to the center-of-mass mode, and the second is a long-distance deviation of the power-law behavior (also most pronounced for small detunings). These effects become worse as the number of defects rises and must be due to the change in character of the phonon modes near the boundary region between the pure ions and the defects. Hence, the aspect ratio of the crystal plays a role in how well the spin-spin couplings are maintained as defects are added to the system, and, as we expect, the

problems are worse for close detuning to the center-of-mass mode.

#### IV. CONCLUSION AND DISCUSSION

In this work, we have developed a general theory and formalism to describe the phonon modes of a single-plane rotating Coulomb crystal in a Penning trap, and used those phonon modes to determine the relevant spin-spin couplings of the system. We find that, in general, the effects of the defects are rather mild even when they result in more than 15% of the lattice sites in the crystal. The biggest effect is in modifying the character of some of the phonon modes in a well-determined fashion. Even so, the effect on the effective spin Hamiltonian generated by a spin-dependent optical force applied to the crystal is rather small, especially if the relative detuning  $\delta$  is held constant during the experiment and the crystal is nearly circular. These results clearly indicate that Penning-trap quantum simulators are robust to the introduction of a number of defects into the system, and hence one need not control the purity to high levels in order to use them as quantum emulators. But deviations are more important for certain shaped crystals, implying that one should go through this type of analysis to ensure that the experiments remain robust against the effects of the defects.

## ACKNOWLEDGMENTS

We thank John Bollinger, Joe Britton, and Brian C. Sawyer for valuable discussions. We also thank Adam Keith and C.-C. Joseph Wang, who worked on the initial stages of this project and created Fig. 1. This work was initially supported under ARO Grant No. W911NF13100019 with

funds from the DARPA OLE Program and was completed under support from the NSF under Grant No. PHY-1314295. J.K.F. further acknowledges support from the McDevitt bequest at Georgetown University. B.Y. also acknowledges support from the Achievement Rewards for College Scientists Foundation.

- 
- [1] R. P. Feynman, *Int. J. Theor. Phys.* **21**, 467 (1981).
  - [2] A. Friedenauer, H. Schmitz, J. T. Glueckert, D. Porras, and T. Schaetz, *Nat. Phys.* **4**, 757 (2008).
  - [3] K. Kim, M.-S. Chang, R. Islam, S. Korenblit, L.-M. Duan, and C. Monroe, *Phys. Rev. Lett.* **103**, 120502 (2009).
  - [4] K. Kim, M.-S. Chang, S. Korenblit, R. Islam, E. E. Edwards, J. K. Freericks, G.-D. Lin, L.-M. Duan, and C. Monroe, *Nature (London)* **465**, 590 (2010).
  - [5] E. E. Edwards, S. Korenblit, K. Kim, R. Islam, M.-S. Chang, J. K. Freericks, G.-D. Lin, L.-M. Duan, and C. Monroe, *Phys. Rev. B* **82**, 060412(R) (2010).
  - [6] R. Islam, E. E. Edwards, K. Kim, S. Korenblit, C. Noh, H. Carmichael, G.-D. Lin, L.-M. Duan, C.-C. Joseph Wang, J. K. Freericks, and C. Monroe, *Nat. Commun.* **2**, 1374 (2011).
  - [7] J. W. Britton, B. C. Sawyer, A. C. Keith, C.-C. Joseph Wang, J. K. Freericks, M. J. Biercuk, H. Uys, and J. J. Bollinger, *Nature (London)* **484**, 489 (2012).
  - [8] B. C. Sawyer, J. W. Britton, A. C. Keith, C.-C. Joseph Wang, J. K. Freericks, H. Uys, M. J. Biercuk, and J. J. Bollinger, *Phys. Rev. Lett.* **108**, 213003 (2012).
  - [9] B. P. Lanyon, C. Hempel, D. Nigg, M. Müller, R. Gerritsma, F. Zähringer, P. Schindler, J. T. Barreiro, M. Rambach, G. Kirchmair, M. Hennrich, P. Zoller, R. Blatt, and C. F. Roos, *Science* **334**, 57 (2011).
  - [10] R. Islam, C. Senko, W. C. Campbell, S. Korenblit, J. Smith, A. Lee, E. E. Edwards, C.-C. J. Wang, J. K. Freericks, and C. Monroe, *Science* **340**, 583 (2013).
  - [11] D. J. Wineland, C. Monroe, W. M. Itano, D. Liebfried, B. E. King, and D. M. Meekhof, *J. Res. Natl. Inst. Stand. Technol.* **103**, 259 (1998).
  - [12] C.-C. Joseph Wang, A. C. Keith, and J. K. Freericks, *Phys. Rev. A* **87**, 013422 (2013).
  - [13] M. J. Biercuk, H. Uys, A. P. VanDevender, N. Shiga, W. M. Itano, and J. J. Bollinger, *Quantum Inf. Comput.* **9**, 920 (2009).
  - [14] T. Hasegawa, M. J. Jensen, and J. J. Bollinger, *Phys. Rev. A* **71**, 023406 (2005).
  - [15] P. Zou, J. Xu, W. Song, and S.-L. Zhu, *Phys. Lett. A* **374**, 1425 (2010).
  - [16] J. D. Baltrusch, A. Negretti, J. M. Taylor, and T. Calarco, *Phys. Rev. A* **83**, 042319 (2011).
  - [17] D. Porras and J. I. Cirac, *Phys. Rev. Lett.* **92**, 207901 (2004).
  - [18] D. A. Baiko, *Phys. Rev. E* **80**, 046405 (2009).
  - [19] See Supplemental Material at <http://link.aps.org/supplemental/10.1103/PhysRevA.88.043434> for movies of the cyclotron phonon modes. Four movies are available for phonon modes for the circular-shaped crystal and four for the oval-shaped crystal. Two of the movies are for the lowest-energy defect motion phonons and two are for the lowest-energy pure ion motion phonons.